Reconstruction of Limited-angle Duel-Energy CT Using Mutual Learning and Cross-estimation (MLCE)

Huayu Zhang[a,b] and Yuxiang Xing[a]

[a]Department of Engineering Physics, Tsinghua University and Key Laboratory of Particle & Radiation Imaging (Tsinghua University), Ministry of Education, 100084, Beijing, China.
[b]Department of Electrical and Computer Engineering, University of Wisconsin Madison, Madison, USA

ABSTRACT

Dual-energy CT (DECT) imaging has gained a lot of attenuation because of its capability to discriminate materials. We proposes a flexible DECT scan strategy which can be realized on a system with general X-ray sources and detectors. In order to lower dose and scanning time, our DECT acquires two projections data sets on two arcs of limited-angular coverage (one for each energy) respectively. Meanwhile, a certain number of rays from two data sets form conjugate sampling pairs. Our reconstruction method for such a DECT scan mainly tackles the consequent limited-angle problem. Using the idea of artificial neural network, we excavate the connection between projections at two different energies by constructing a relationship between the linear attenuation coefficient of the high energy and that of the low one. We use this relationship to cross-estimate missing projections and reconstruct attenuation images from an augmented data set including projections at views covered by itself (projections collected in scanning) and by the other energy (projections estimated) for each energy respectively.

Validated by our numerical experiment on a dental phantom with rather complex structures, our DECT is effective in recovering small structures in severe limited-angle situations. This DECT scanning strategy can much broaden DECT design in reality.

Keywords: Limited-angle reconstruction, Multi-energy CT, prior, sparsity, neural network

1. INTRODUCTION

Dual energy Computed Tomography (DECT) was proposed in 1970s and now becomes increasingly popular because of the development of X-ray detectors and the emergence of new system designs in X-ray imaging. Free from the drawbacks of conventional CT such as beam hardening and limited contrast, DECT enables the differentiation of materials, especially those with similar attenuation at certain energies.[1] These features make DECT of high diagnostic value. Now, DECT has many clinical applications such as in abdomen[2] and pulmonary diseases .[3]

Generally speaking, the number of data doubles when imaging at two energies. For example, a fan-beam CT usually requires projection data over an angular range of 180° plus the fan angle (δ_{fan}). Therefore, a fan-beam DECT needs at least two sets of $180° + \delta_{\text{fan}}$ projections. Different system designs for DECT have been applied in practice. A dual-source DECT[4] using two sets of sources/detectors simultaneously acquires projection data at two energy spectra. An energy-dispersive DECT uses novel photon counting detectors with the ability of energy-dispersive X-ray detection.[5] A rapid-kVp-switching DECT scanner needs an X-ray source with the ability of swift switching between two voltages.[6] Obtaining high quality dual-energy images with these methods depends heavily on advanced devices and increases cost. Recently, L. Shen *et al*[7] proposed a segmental multi-energy CT

Further author information: Send correspondence to Yuxiang Xing
Huayu Zhang was in the department of engineering physics, Tsinghua university and now is in the department of electrical and computer engineering, university of Wisconsin Madison.: E-mail: zhuayu@wisc.edu, Telephone: 1 608 770 1803
Yuxiang Xing: E-mail: xingyx@mail.tsinghua.edu.cn, Telephone: +86 (10)62782510

(SegMECT) scan strategy which could easily implement DECT using a traditional scanner and detector with only one step of change to its tube potential. It separates a 360° scan orbit into two parts. Low-energy X-ray beams are applied in one part and high-energy X-ray beams in the other. It is obvious that less data acquisition has a potential to reduce dose, cost, as well as acquisition and reconstruction time. The segmental DECT can reduce the data requirement to half.

Dose has been a critical issue in X-ray imaging. People have devoted a lot of effort to reduce dose. One typical way is less tube current. Reconstruction methods [8,9] have been published to improve reconstruction by applying statistical models. Limited view angle could be another way to cut down dose. However, it needs the support of appropriate reconstruction methods. Normally, when the angular coverage of a fan beam scan are less than 180° plus the fan angle, the reconstruction violates data sufficient condition.[10,11] Reconstruction images will suffer from artifacts caused by the limited angle. Smaller the angular coverage, more severe the artifacts. In Shen's method, the total angular range covered by the dual-energy X-ray beams has to be more than 180° plus a fan angle so that a reasonable prior can be built to guide the reconstruction. In this work, we would like to explore the possibility of further reducing the angular coverage in such a Segmental DECT system. The main difficulty is in solving the limited-angle problem.

Limited angle CT scans widely exist in the real world subjected to the low dose requirement,[12] short exposure time[13] and other physical limitations. Fundamentally, this kind of scan provides insufficient data for reconstruction. Many methods have been published for CT reconstruction with insufficient data. A well recognized and successful type is introducing sparsity priors based on the theory of compressed sensing.[14] E. Y. Sidky *et al*[15,16] proposed a reconstruction strategy combining traditional algebraic reconstruction techniques (ART) with a total-variation (TV) regularization on the image domain.

$$\boldsymbol{\mu} = \arg\min_{\boldsymbol{\mu}\in\mathbb{R}^N} \|\boldsymbol{\mu}\|_{TV} \quad s.t. \quad \boldsymbol{H}\boldsymbol{\mu} = \boldsymbol{p} \tag{1}$$

where $\boldsymbol{\mu} \in \mathbb{R}^N$ is the image representing the linear attenuation coefficients of the object, $\boldsymbol{H} \in \mathbb{R}^{M\times N}$ is the system matrix and $\boldsymbol{p} \in \mathbb{R}^M$ is the projection data. This method can reconstruct a 256×256 Shepp-Logan phantom with only 20 views. Based on this work, X. Jin *et al*[17] proposed anisotropic total variation (ATV), which showed nice results for limited-angle problems. H. Gao *et al*[18] explored the coherence of images at multi-energy channels and proposed a joint sparsity and low rank constraint model. G. H. Chen *et al*[19] applied compressed sensing to dynamic imaging and developed the prior image constrained compressed sensing (PICCS) method. PICCS is also used for reconstruction of a slow-kVp-switching DECT .[20] K. Kim *et al*[21] designed a patch-based low-rank penalty for sparse view spectral CT. These methods performs quite well for few-view problems and limited angle problems with relatively simple structures. We intend to incorporate compressed sensing methods in this work, aiming at reducing the sampling projections further on by leveraging both the special data structure on DECT and the popular sparsity constraints.

In this paper, we propose a more flexible DECT scanning strategy by extending the idea of SegMECT.[7] Our new DECT makes one arc of scan at each energy like SegMECT, but the transition region of tube potential between these two arcs is wider and deposits no X-ray dose. Most importantly, less angular coverage is needed than SegMECT.[7] An additional requirement is that there must exist some conjugate sampling pairs between two data sets. We refer this new DECT as two-arc DECT (TA-DECT). A novel reconstruction method is designed for our TA-DECT. In this method, we explore using the artificial neural network to establish a mapping between the linear attenuation coefficients of two energies, and then cross-estimate the missing projection data of the two energy channels. Thus we augment the projection data to the range covered by both high-energy and low-energy X-rays for each energy. The final reconstruction is obtained from the augmented data together with total-variation constraints. We call this method Mutual Learning and Cross-Estimation (MLCE).

To summarize, our work has the following contributions,

1. We reduce the coverage angle of each energy to 90° in DECT, nearly half of that in conventional DECT.
2. We solve the limited-angle problem from a novel view. By studying the relationship between the linear attenuation coefficients at the two energies, we can recovery part of the data not sampled when scanning, thus mitigating the limited-angle artifacts to some extent.

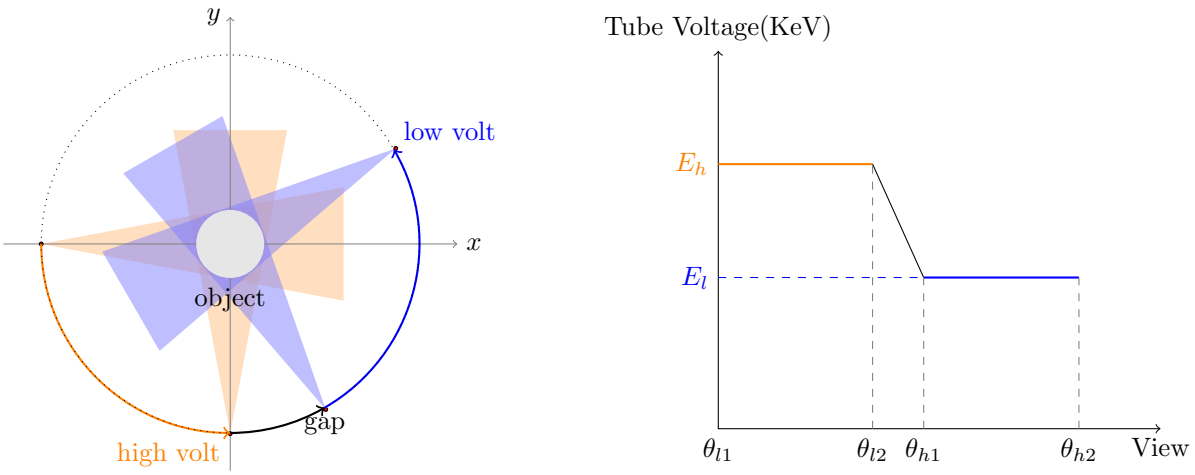

Figure 1: TA-DECT scanning. The transition gap between the scans is for switching a high tube voltage to a low tube voltage as in practical situation.

The rest of the paper is organized as follows. We present the detailed design of the scanning strategy and the reconstruction algorithm (MLCE) is described in § 2. We evaluate and discuss our approach with numerical simulations in § 3. § 4 concludes our work.

2. METHODOLOGY

2.1 Sampling Strategy

We extend the easy-to-implement SegMECT scanning strategy[7] to configure a new DECT scan. As shown in Figure 1, fan-beam projection data are acquired in two arcs. For each arc, either high- or low-energy X-ray is used. Partial of the data from these two arcs should form a number of conjugate sampling pairs (Figure 4), and a voltage-transition gap between the two arcs eases the implementation of such a slow-kVp-switching system. The advantage of such a scan is in four aspects:

1. Reducing the angular coverage of the two arcs could linearly reduce the total dose delivered to a scanned object;
2. No dosage is delivered during the tube potential change, which means no extra dose besides the X-rays from two stages of determinant tube potential;
3. The gap between two arcs can be wide enough for X-ray tube to complete the potential change smoothly;
4. This configuration can fit in the situations with physical blockage in completing a full circular rotation.

2.2 Reconstruction Algorithm

Many efforts have been done to model the relationship between attenuation maps under different energies. G. Hao *et al*[18] modeled the relationship with low rank, and L. Shen *et al*[7] used the similarity of edge structure. Here, we would like to build a mapping between the projections at different energies,

$$\varphi_{E_1,E_2} : \boldsymbol{p}_{E_1} \rightarrow \boldsymbol{p}_{E_2} \tag{2}$$

where $\boldsymbol{p}_{E_1}, \boldsymbol{p}_{E_2}$ denote the projections at energy E_1 and energy E_2. E_1 can be the high energy while E_2 the low energy and vice versa. With this mapping we can cross-estimate missing data to improve final reconstructions. However, the relationship between projection data at different energies is not apparent. Therefore, we establish an indirect mappings in image domain and obtain φ_{E_1,E_2} through a forward projection. Let $\boldsymbol{\mu}_{E_1}$ and $\boldsymbol{\mu}_{E_2} \in \mathcal{R}^N$

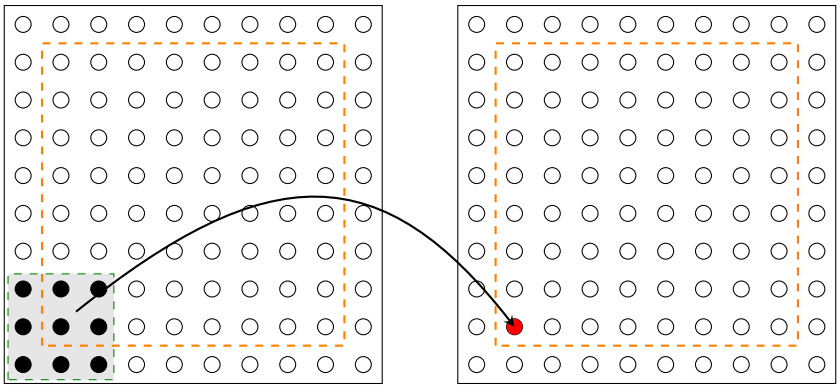

Figure 2: $\boldsymbol{\mu}_{E_1} \mapsto \boldsymbol{\mu}_{E_2}$ mapping. A mapping is established from a set of $d \times d$ templates cropped from $\boldsymbol{\mu}_{E_1}$ to the center of the window from $\boldsymbol{\mu}_{E_2}$ with an artificial neural network. All the pixels in the orange rectangle together with their neighbors in a $d \times d$ window are used to train the neural network.

denoting the images reconstructed from $\boldsymbol{p}_{E_1}$ and $\boldsymbol{p}_{E_2}$, and $\psi_{E_1,E_2} : \boldsymbol{\mu}_{E_1} \mapsto \boldsymbol{\mu}_{E_2}$ denote the mapping between the linear attenuation coefficient images at different energies, we have

$$\boldsymbol{p}_{E_2} = \varphi_{E_1,E_2}(\boldsymbol{p}_{E_1}) = \mathcal{R}(\psi_{E_1,E_2}(\mathcal{R}^{-1}(\boldsymbol{p}_{E_1}))) \tag{3}$$

where $\mathcal{R}$ is a projection operator.

In practice, we can perform the mapping ψ_{E_1,E_2} pixel by pixel,

$$\mu_{E_2}(n) = \psi_{E_1,E_2}(\mu_{E_1}(n)) \tag{4}$$

where n indexing a pixel. Therefore ψ_{E_1,E_2} is actually a mapping of linear attenuation coefficients between two energies. Ideally speaking, we need two accurate linear attenuation maps for building an exact mapping. However, those are not available. Hence, we try to study the relationship of linear attenuation coefficients under different energies from limited information. To increase the adaptivity and robustness, a $d \times d$ window including the neighbors of a pixel $\boldsymbol{n}$ from energy E_i instead of $\mu_{E_i}(n)$ itself alone is used as the input and the value of pixel n from energy $E_{i'}$ as the target (Figure 2). Thus Eq. 4 becomes

$$\mu_{E_2}(n) = \psi_{E_1,E_2}\left(\mu_{E_1}(\Omega)\right), \ \Omega = \text{Neighbour}(n) \tag{5}$$

The mapping can be established by fitting if the relationship is simple enough. The challenges lie in the fact that different objects have different linear attenuation coefficients and that the relationship of linear attenuation coefficients between dual energies does not conform a fixed pattern like linear or quadratic relation. Taking into consideration all these factors, we use an artificial neural network (ANN)[22,23](Figure 3) to study the relationship online. The images reconstructed from conjugate sampling pairs of both energies serve as $\boldsymbol{\mu}_{E_1}$ and $\boldsymbol{\mu}_{E_2}$ for ANN training.

2.3 Mutual Learning and Cross-Estimation (MLCE) Reconstruction

In our notation, the high energy projection data $\boldsymbol{p}_h(\theta, \delta)$ is acquired over an angular range $R_h = [\theta_{h1}, \theta_{h2}]$ and the low energy one $\boldsymbol{p}_l(\theta, \delta)$ over another angular range $R_l = [\theta_{l1}, \theta_{l2}]$, where θ denotes the angle of the central ray and δ the fan angle from the central ray, as showed in Figure 4.

For the TA-DECT reconstruction, we have

$$\boldsymbol{H}_h\boldsymbol{\mu}_h = \boldsymbol{p}_h \tag{6}$$
$$\boldsymbol{H}_l\boldsymbol{\mu}_l = \boldsymbol{p}_l \tag{7}$$

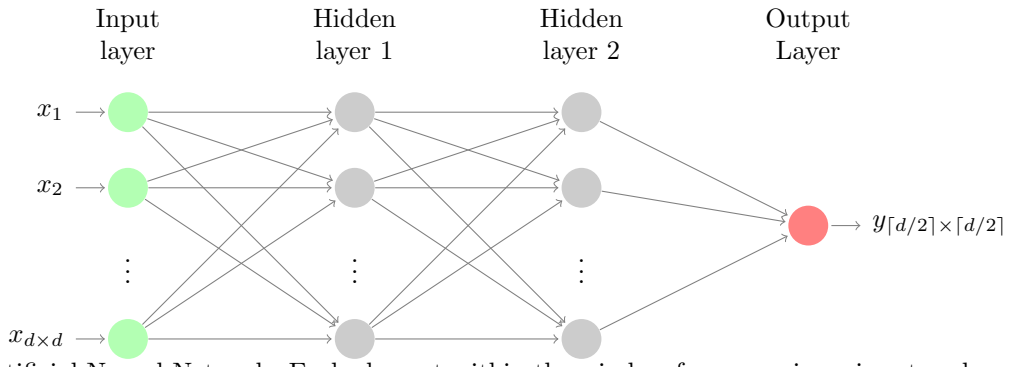

Figure 3: Artificial Neural Network. Each element within the window from $\boldsymbol{\mu}_{E_1}$ is an input node and $\boldsymbol{\mu}_{E_2}(n)$ at the center of the window is the output node.

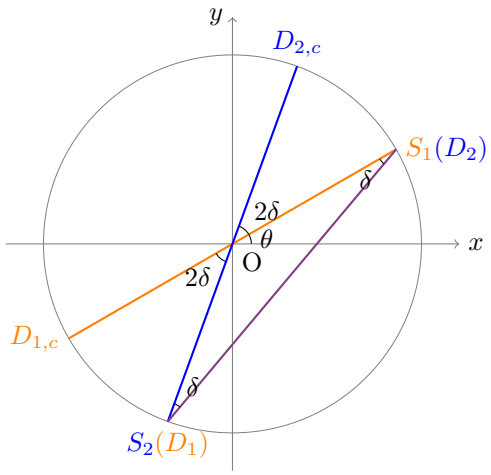

Figure 4: Illustration of conjugate sampling pairs in fan-beam CT. The projection line $S_1D_1(\theta,\delta)$ and $S_2D_2(\theta+\pi+2\delta,-\delta)$ are conjugate sampling pairs.

where $\boldsymbol{H}_h \in \mathcal{R}^{M_h\times N}$ (resp. $\boldsymbol{H}_l \in \mathcal{R}^{M_l\times N}$) is the system matrix for high (resp. low) energy projection, $\boldsymbol{\mu}_h, \boldsymbol{\mu}_l \in \mathcal{R}^N$ are the attenuation images to be reconstructed, and $\boldsymbol{p}_h \in \mathcal{R}^{M_h}$ (resp. $\boldsymbol{p}_l \in \mathcal{R}^{M_l}$) is the projection data of high (resp. low) energy.

We first establish a mapping of linear attenuation coefficients between dual energies by training our artificial neural network using the conjugate sampling pairs. Then we cross-estimate the missing projection data with the trained neural network. With augmented data, we can get better images than those independently reconstructed from single-energy data. The details are described in the following. The flowchart of our reconstruction method is presented in Figure 5.

2.3.1 Mapping

As showed in Figure 4, the ray path of S_1D_1 and S_2D_2 are exactly the same, i.e.,

$$p(\theta,\delta) = p(\theta+\pi+2\delta,-\delta) \tag{8}$$

(θ,δ) and $(\theta+\pi+2\delta,-\delta)$ are referred as a conjugate sampling pair. In the design of our scanning strategy, the existence of conjugate sampling pairs is ensured. Let $\boldsymbol{p}_h^{\text{cgs}}$ and $\boldsymbol{p}_l^{\text{cgs}}$ denote the conjugate sampling pairs from high or low energy projections. We use $\boldsymbol{p}_h^{\text{cgs}}$ and $\boldsymbol{p}_l^{\text{cgs}}$ to reconstruct images $\boldsymbol{\mu}_h^{\text{cgs}}, \boldsymbol{\mu}_l^{\text{cgs}}$, which are the training data for ANN to establish the dual-energy mappings.

Though degraded heavily by severe artifacts, $\boldsymbol{\mu}_h^{\text{cgs}}$ and $\boldsymbol{\mu}_l^{\text{cgs}}$ share the same structure of the object as well as same artifacts. They also contain the information of intensity difference in each pixel, which hopefully will

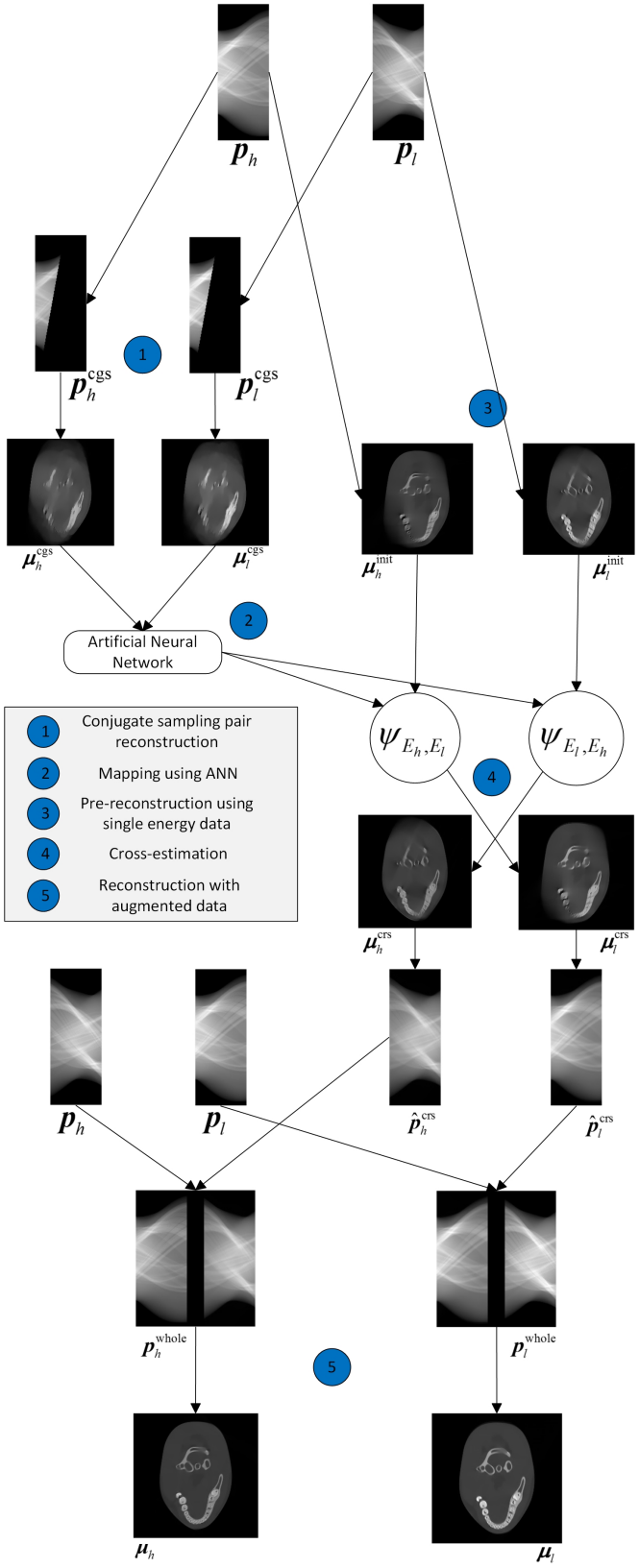

Figure 5: Chain of processing steps in Mutual Learning and Cross-Estimation (MLCE)

be implicitly modeled by the mapping. Therefore, two mappings $\psi_{E_h,E_l} : \boldsymbol{\mu}_h \rightarrow \boldsymbol{\mu}_l$ and $\psi_{E_l,E_h} : \boldsymbol{\mu}_l \rightarrow \boldsymbol{\mu}_h$ are established in our reconstruction method (schematically illustrated in Figure 2 and Figure 3).

2.3.2 Estimation of Missing Projections

After the ANN learns the dual-energy mappings, we implement a pre-reconstruction, which independently gets initiative estimation of attenuation image from projection data of each energy, using the reconstruction algorithm OSSART[24] + TV.[15]

$$\boldsymbol{\mu}_h^{\text{init}} = \arg\min_{\boldsymbol{\mu}_h} \|\boldsymbol{\mu}_h\|_{TV} \quad s.t. \quad \boldsymbol{H}_h\boldsymbol{\mu}_h = \boldsymbol{p}_h \tag{9}$$

$$\boldsymbol{\mu}_l^{\text{init}} = \arg\min_{\boldsymbol{\mu}_l} \|\boldsymbol{\mu}_l\|_{TV} \quad s.t. \quad \boldsymbol{H}_l\boldsymbol{\mu}_l = \boldsymbol{p}_l \tag{10}$$

The reconstruction $\boldsymbol{\mu}_h^{\text{init}}$ we obtain is from data covering the angular range R_h, where the low-energy projection data is lacking. As we have the mapping $\psi_{E_h,E_l} : \boldsymbol{\mu}_h \rightarrow \boldsymbol{\mu}_l$, we can estimate the attenuation image of low energy,

$$\hat{\boldsymbol{\mu}}_l^{\text{crs}} = \psi_{E_h,E_l}(\boldsymbol{\mu}_h^{\text{init}}) \tag{11}$$

Let $\hat{\boldsymbol{p}}_l^{\text{crs}}$ denote our estimation of the low-energy projection data at the views of R_h, we have

$$\hat{\boldsymbol{p}}_l^{\text{crs}} = \boldsymbol{H}_h\hat{\boldsymbol{\mu}}_l^{\text{crs}} \tag{12}$$

In the same way, the high-energy image in the angular range R_l is also estimated,

$$\hat{\boldsymbol{\mu}}_h^{\text{crs}} = \psi_{E_l,E_h}(\boldsymbol{\mu}_l^{\text{init}}) \tag{13}$$

With a fan-beam projection, we get

$$\hat{\boldsymbol{p}}_h^{\text{crs}} = \boldsymbol{H}_l\hat{\boldsymbol{\mu}}_h^{\text{crs}} \tag{14}$$

Thus, we have estimated the projection of low energy over the angular range R_h and the projection of high energy over the angular range R_l. Let $\boldsymbol{p}_h^{\text{whole}}$ and $\boldsymbol{p}_l^{\text{whole}}$ denote the whole data on R_l and R_h,

$$\boldsymbol{p}_h^{\text{whole}} = \begin{pmatrix} \boldsymbol{p}_h \\ \hat{\boldsymbol{p}}_h^{\text{crs}} \end{pmatrix} \qquad \boldsymbol{p}_l^{\text{whole}} = \begin{pmatrix} \hat{\boldsymbol{p}}_l^{\text{crs}} \\ \boldsymbol{p}_l \end{pmatrix} \tag{15}$$

This estimation almost doubles the projection data compared with the data acquired, thus could greatly help us to improve the image quality of reconstruction.

2.3.3 Reconstruction with augmented data

With the augmented data $\boldsymbol{p}_h^{\text{whole}}$ and $\boldsymbol{p}_l^{\text{whole}}$, we reconstruct the final results. Because the following processing is for both low and high energy data, we omit the subscriptions in the equations and expressions here. Let

$$\boldsymbol{H} = \begin{pmatrix} \boldsymbol{H}_h \\ \boldsymbol{H}_l \end{pmatrix} \tag{16}$$

we have

$$\boldsymbol{H}\boldsymbol{\mu} = \boldsymbol{p}^{\text{whole}} \tag{17}$$

We solve Eq. 17 with a TV regularization.

$$\arg\min_{\boldsymbol{\mu}} \|\boldsymbol{\mu}\|_{TV} \quad s.t. \quad \boldsymbol{H}\boldsymbol{\mu} = \boldsymbol{p} \tag{18}$$

Methods to solve Eq. 18 are reported by many aricles.[15,16]

(a) Dental phantom

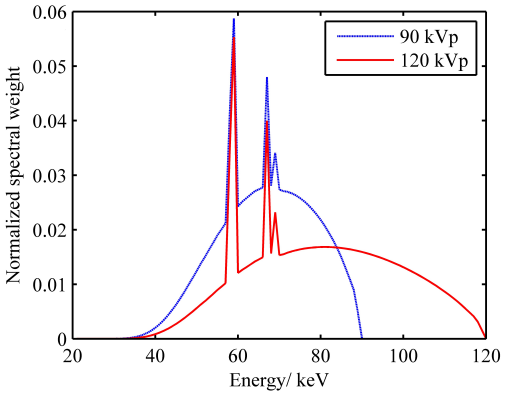

(b) Energy spectra

Figure 6: Experimental setup. (a) is the dental phantom and (b) is the spectra of high energy 120kVp and low energy 90kVp for this study.

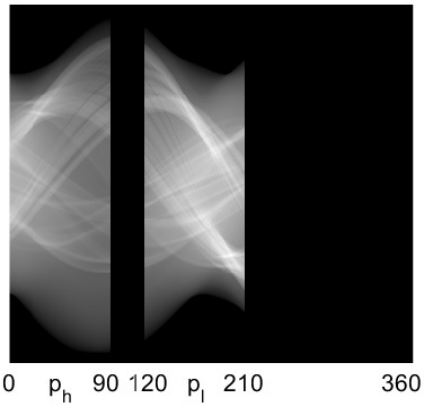

Figure 7: Overall TA-DECT sinogram of limited angle projections. Range $V_{\text{high}} = [0°, 90°)$ is covered by the high-energy projections and Range $V_{\text{low}} = [120°, 210°)$ is covered by the low-energy ones.

3. EXPERIMENTAL STUDY

We conducted a simulation study on a numerical dental phantom (Figure 6(a)) to validate our DECT reconstruction method based on Mutual Learning and Cross-Estimation (MLCE).

Fan-beam projections with slight noise under two X-ray energy spectra as shown in Figure 6(b) are simulated. Overall, 960 detectors are aligned on a 300 mm line. The field of view (FOV) is 200 mm $\times$ 200 mm. The distance between the source and the center of FOV is 500 mm. The distance from the center of FOV to the linear detectors is 300 mm. For complete data in each energy, the projection data was acquired over $0° \sim 360°$ with an increment of $1°$. The data in the range R_h of the high-energy data and R_l of the low-energy data are picked for TA-DECT. In this study, we set $V_{\text{high}} = [0°, 90°), V_{\text{low}} = [120°, 210°)$, leaving a $30°$ gap for voltage switch. The resulting sinogram in total from TA-DECT are shown in Figure 7.

An accurate training using the neural network is a pre-request for cross estimation of projection data. The number of conjugate sampling pairs for training and the size of inputs of the neural network should be taken into consideration. More conjugate sampling pairs enable better training, but cause less available projection data in our final reconstruction because of our sampling strategy and reconstruction method. Therefore, trade off should be made to use less conjugate sampling pairs while keeping a good training. The basic request for a good training is that images reconstructed from conjugate pairs $(\boldsymbol{\mu}_l^{\text{cgs}}, \boldsymbol{\mu}_h^{\text{cgs}})$ have an approximal relationship and preserve some edge details. Experiments were conducted to determine the proper number of conjugate sampling pairs. We experimented on $11\%, 22\%, 33\%, 44\%$ projection pairs forming conjugate sampling pairs for reconstruction. As shown in Figure 8, 33% projection pairs are enough for an acceptable approximation.

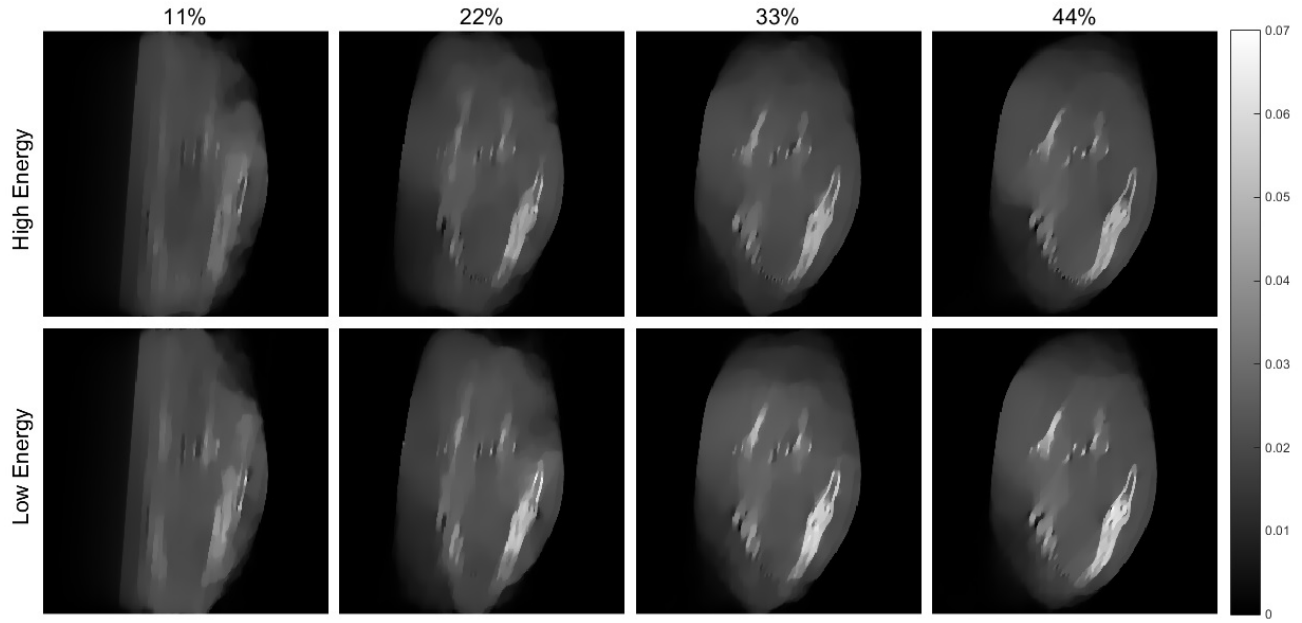

Figure 8: Conjugate Sampling Pair Reconstruction. Upper row: High energy, Lower row: Low energy; From left to right: reconstruction using $11\%, 22\%, 33\%, 44\%$ pairs of views forming conjugate sampling pairs. Display window:$[0, 0.07]\text{mm}^{-1}$.

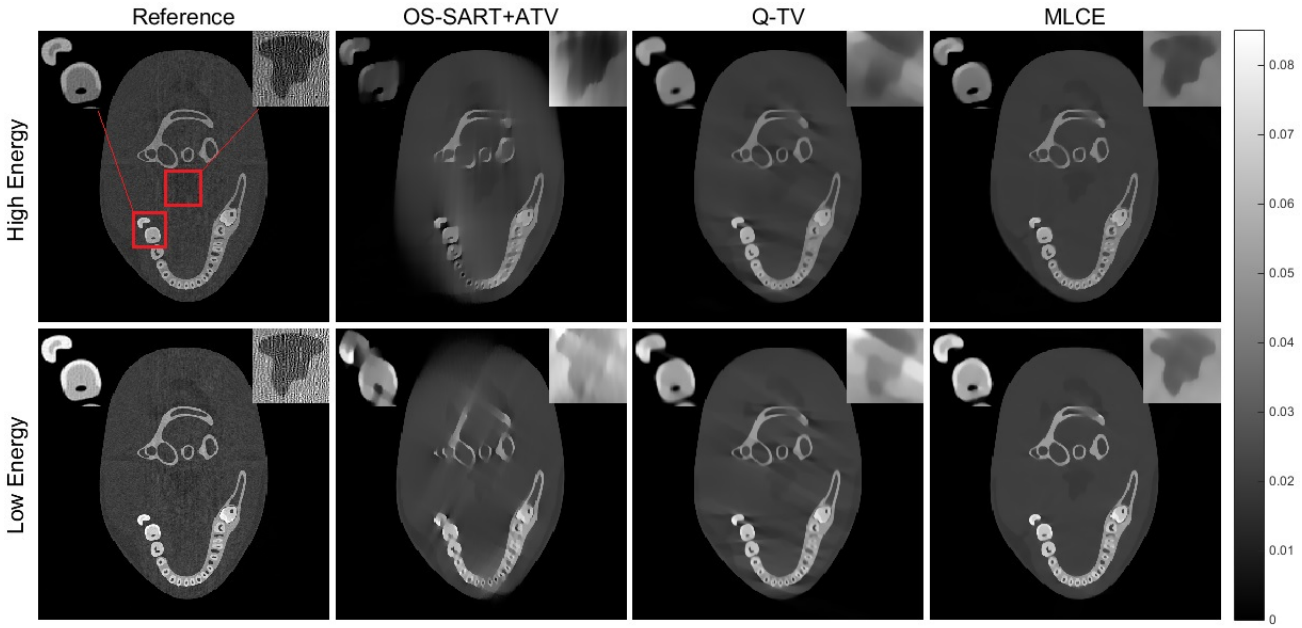

Figure 9: Reconstruction from DECT scans. Upper row: results of high energy. Bottom row: results of low energy. From left to right: OS-SART with complete data, independent OS-SART+ATV, Q-TV, MLCE with data range $V_{\text{high}} = [0°, 90°), V_{\text{low}} = [120°, 210°)$. Display window:$[0, 0.085]\text{mm}^{-1}$. For the zoom-in teeth ROI, the display window is $[0.03, 0.085]\text{mm}^{-1}$. For the zoom-in soft tissue ROI, the display window is $[0.015, 0.025]\text{mm}^{-1}$.

.

If the training data for the neural network and the pre-reconstruction data for estimation are perfect, a 1×1 window will yield the best performance. However, as both data are imperfect in our method, a $d \times d, d > 1$ window may be more feasible, but a large d will cause blur in output images. We experimented on different

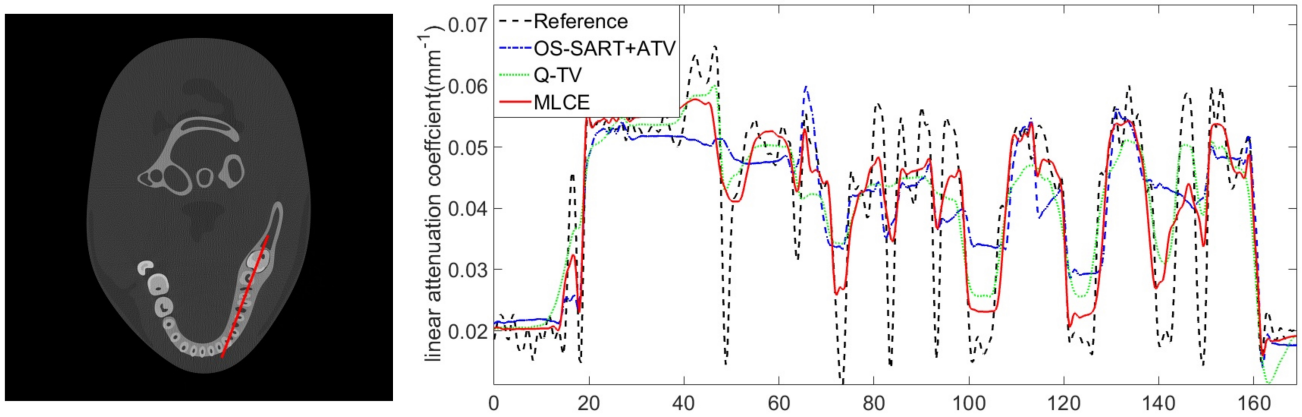

(a) Profiles at high energy.

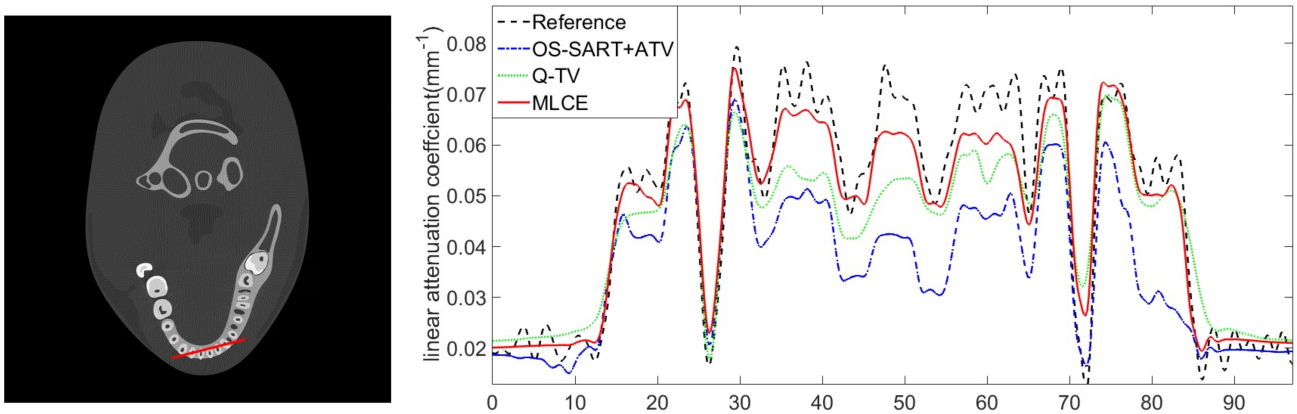

(b) Profiles at low energy.

Figure 10: Profiles of the reconstructions along the red line as indicated in the left image. In most areas, the profile of reconstructions from MLCE is the closest to the reference. On the contrary, the independent OS-SART+ATV and Q-TV reconstructions lose some edge details and are heavily affected by limited angle artifacts.

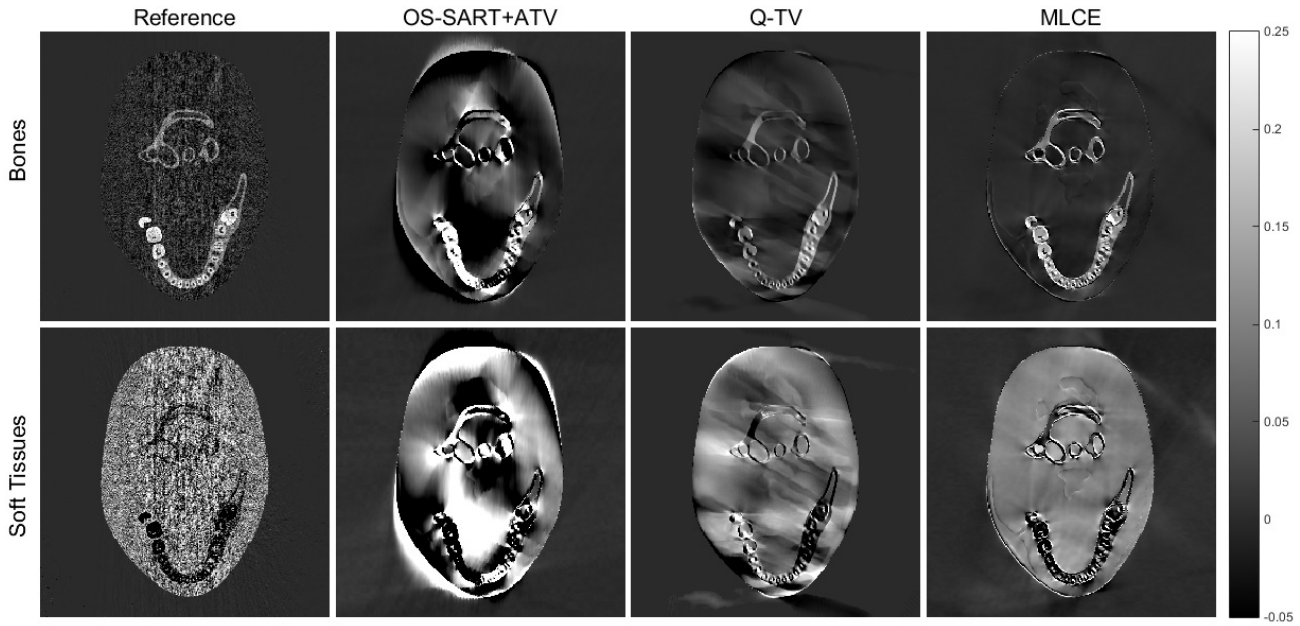

Figure 11: DECT decomposition of bones and soft tissues. Upper row: Bone images. Bottom row: Soft tissue images. From left to high: OS-SART with complete data, independent OS-SART+ATV, Q-TV, MLCE with data range $V_{\text{high}} = [0°, 90°), V_{\text{low}} = [120°, 210°)$. Display window:$[-0.05, 0.25]\text{cm}^{-1}$

window size: 1×1, 3×3, 5×5 for the input of our neural network. 33% projection pairs forming conjugate sampling pairs were used for training and right-angled projections at dual energies are used for testing. The rooted mean square error (RMSE) are shown in Table 1. The 3×3 window performs best.

Table 1: Rooted mean square error of mapping with different window sizes.

Mapping	1×1	3×3	5×5
$\varphi : p_l \to p_h$	0.048	0.035	0.046
$\varphi : p_h \to p_l$	0.023	0.023	0.032

Based on our experimental results, the neural network we used had two hidden layers, both with 10 nodes. 33% projections at both energies forming conjugate pairs were used for training the neural network. The window size for training ANN was 3×3. OS-SART together with a TV constraint was used for our final reconstruction. We set relaxation factor $\lambda = 0.8$, the number of iterations $N = 100$. For TV regularization, the number of iterations $N_{\text{TV}} = 20$, the gradient descent speed $\alpha = 0.2$. The grids of reconstruction image were 512×512.

We compared our algorithm with the Q-TV method[7] and independent reconstruction (OS-SART+ATV)[17] for each-energy given the same projection data. The results from projections within $V_{\text{high}} = [0°, 90°)$ and $V_{\text{low}} = [120°, 210°)$ are presented in Figure 9. In the figure, the top row presents the images reconstructed from the high-energy projection data and the bottom row from the low-energy projection data. From left to right columns are the images reconstructed by OS-SART with complete data, independent reconstruction using OS-SART+ATV, Q-TV and our MLCE reconstruction with TA-DECT data. Figure 10 show the profiles along the red lines in the left images at both energies. We further examined the material decomposition using these attenuation image pairs. The basis-material decomposition method same as in[7] was used. The resulting images of bones and soft tissue components from the image pairs in Figure 9 are shown in Figure 11. Obviously, the error in attenuation images is further amplified in the component images. In both OS-SART+ATV reconstruction and Q-TV reconstruction cases, component images are biased by significant limited angle artifacts though TV regulation smooth the noise. Compared to them, our MLCE reconstruction gives much accurate information of the bones and soft tissue composition.

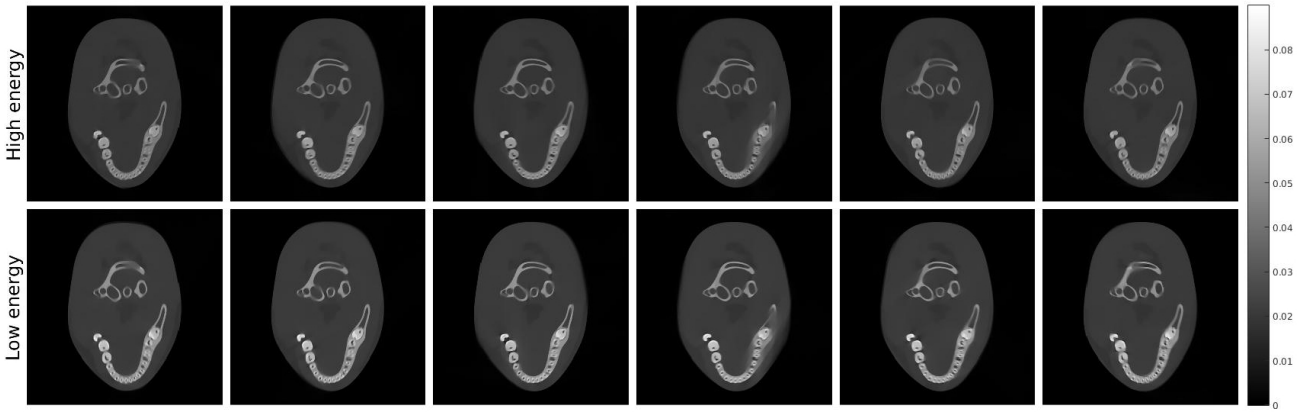

Figure 12: Comparison of reconstruction under different view configuration. From left to right are results from Case I ($V_{\text{high}} = [1°, 90°], V_{\text{low}} = [121°, 210°]$), case II ($V_{\text{high}} = [31°, 120°], V_{\text{low}} = [151°, 240°]$), case III ($V_{\text{high}} = [61°, 150°], V_{\text{low}} = [181°, 270°]$), case IV ($V_{\text{high}} = [91°, 180°], V_{\text{low}} = [211°, 300°]$), case V ($V_{\text{high}} = [121°, 210°], V_{\text{low}} = [241°, 330°]$), and case VI ($V_{\text{high}} = [151°, 240°], V_{\text{low}} = [271°, 360°]$.

To evaluate the robustness of our method at different sampling views. We examine six different sampling configurations with the first sampling view set as ($V_{\text{high}} = [1°, 90°], V_{\text{low}} = [121°, 210°]$) and the others a 30° shift of its right previous one. The reconstruction results under these view settings are shown in Figure 12. In all six cases, the blurred directions and regions are different. This is because the data insufficiency happens in different directions. When scanning, people can configure the view settings so that the blurring does not emerge along the important directions.

4. DISCUCSSION AND CONCLUSION

This paper presented a new scanning strategy for DECT to reduce the data requirement and ease DECT implementation. Compared to a common DECT, more that 50% of data, which could also mean dose reduction, are saved based on our new MLCE reconstruction method. The main idea is to use a mutual learning strategy based on artificial neural network to solve the problem of reconstruction from limited-angle projections. As the data acquisition strategy for this algorithm is easy to implement with no items like energy-dispersive detectors and fast-kVp-switching sources, it is very promising in practical applications.

The proposed method is numerically tested on a dental phantom. The results demonstrated that our method is superior to independent OS-SART+ATV reconstruction with each energy projection data and the Q-TV method. The general regularizations like TV and ATV constraints does not yield good results for such a limited-angle problem. In the dental CT reconstruction, OS-SART+ATV suffers blurring artifacts along the directions where no X-ray goes perpendicularly through it. Some tiny bones are doomed to be blurred instead of being preserved by TV regularization. Q-TV loses its power when no good structural prior is available. The significant information missing because of the severe insufficiency of angular views, is very hard to repair with these general prior information and constraints, especially for objects with complex structures.

Considering this, our work deals with the limited-angle reconstruction problem by augmenting the projection data. For $V_{\text{high}} = [0°, 90°), V_{\text{low}} = [120°, 210°)$, the data are insufficient,[10,11] and thus we suffer blurring artifacts along the directions of the gap $[90°, 120°)$. However, with a 150° angular range covered, it is much better than the angular coverage from a single energy projection which is only 90°. Therefore, our MLCE method is more accurate, which is helpful to gain good material decomposition images (Figure 11).

Moreover, our MLCE method is compatible with other compressed sensing methods. It can be regarded as a pre-processing step. In our experiment, the TV constraint is used because the angular coverage by two arcs together is still insufficient. However, the TV constraint could be unnecessary when angular coverage of augmented data is sufficient.

Obtaining the relationship between the linear attenuation coefficients of two energies accurately is the key of our method. This relationship is not linear and does not have explicit regularity because of the complexity and uncertainty of materials in scanned objects. Therefore, we use the artificial neural network to learn this relationship online, which requires conjugate sampling pairs in the projection data. The idea can be easily extended to other imaging geometry such as few-view as long as conjugate sampling pairs available. Neural network is a powerful tool for nonlinear mapping. We use a neural network with two hidden layers and 10 nodes in each layer in this study. Further work can be done to design a more efficient neural network custom for the mapping in DECT or even multi-energy CT.

Acknowledgment

This work is supported by grants from the National Natural Science Foundation of China (No. 11275104 and 11435007). We would like to thank Le Shen for his support and helpful discussions.

REFERENCES

[1] Johnson, T. R., Krauss, B., Sedlmair, M., Grasruck, M., Bruder, H., Morhard, D., Fink, C., Weckbach, S., Lenhard, M., Schmidt, B., et al., "Material differentiation by dual energy ct: initial experience," *European radiology* **17**(6), 1510–1517 (2007).

[2] Heye, T., Nelson, R. C., Ho, L. M., Marin, D., and Boll, D. T., "Dual-energy ct applications in the abdomen," *American Journal of Roentgenology* **199**(5_supplement), S64–S70 (2012).

[3] Kang, M.-J., Park, C. M., Lee, C.-H., Goo, J. M., and Lee, H. J., "Dual-energy ct: Clinical applications in various pulmonary diseases 1," *Radiographics* **30**(3), 685–698 (2010).

[4] Flohr, T., Bruder, H., Stierstorfer, K., Petersilka, M., Schmidt, B., and McCollough, C., "Image reconstruction and image quality evaluation for a dual source ct scanner," *Medical physics* **35**(12), 5882–5897 (2008).

[5] Iwanczyk, J. S., Nygard, E., Meirav, O., Arenson, J., Barber, W. C., Hartsough, N. E., Malakhov, N., and Wessel, J. C., "Photon counting energy dispersive detector arrays for x-ray imaging," *Nuclear Science, IEEE Transactions on* **56**(3), 535–542 (2009).

[6] Goodsitt, M. M., Christodoulou, E. G., and Larson, S. C., "Accuracies of the synthesized monochromatic ct numbers and effective atomic numbers obtained with a rapid kvp switching dual energy ct scanner," *Medical physics* **38**(4), 2222–2232 (2011).

[7] Shen, L. and Xing, Y., "Multienergy ct acquisition and reconstruction with a stepped tube potential scan," *Medical physics* **42**(1), 282–296 (2015).

[8] Sukovic, P. and Clinthorne, N. H., "Penalized weighted least-squares image reconstruction for dual energy x-ray transmission tomography," *IEEE Trans. Med. Imaging* **19**(11), 1075–1081 (2000).

[9] Zhang, R., Thibault, J., Bouman, C. A., Sauer, K. D., and Hsieh, J., "Model-based iterative reconstruction for dual-energy x-ray CT using a joint quadratic likelihood model," *IEEE Trans. Med. Imaging* **33**(1), 117–134 (2014).

[10] Tuy, H. K., "An inversion formula for cone-beam reconstruction," *SIAM Journal on Applied Mathematics* **43**(3), 546–552 (1983).

[11] Li, L., Kang, K., Chen, Z., Zhang, L., Xing, Y., Yu, H., and Wang, G., "An alternative derivation and description of smith's data sufficiency condition for exact cone-beam reconstruction," *Journal of X-Ray Science and Technology* **16**(1), 43–49 (2008).

[12] Yu, L., Liu, X., Leng, S., Kofler, J. M., Ramirez-Giraldo, J. C., Qu, M., Christner, J., Fletcher, J. G., and McCollough, C. H., "Radiation dose reduction in computed tomography: techniques and future perspective," *Imaging in medicine* **1**(1), 65–84 (2009).

[13] Jin, X., Li, L., Chen, Z., Zhang, L., and Xing, Y., "Motion-compensated reconstruction method based on rigid motion model with multi-object," *Tsinghua Science & Technology* **15**(1), 120–126 (2010).

[14] Foucart, S. and Rauhut, H., [*A mathematical introduction to compressive sensing*], Springer (2013).

[15] Sidky, E. Y., Kao, C.-M., and Pan, X., "Accurate image reconstruction from few-views and limited-angle data in divergent-beam ct," *Journal of X-ray Science and Technology* **14**(2), 119–139 (2006).

[16] Sidky, E. Y. and Pan, X., "Image reconstruction in circular cone-beam computed tomography by constrained, total-variation minimization," *Physics in Medicine and Biology* **53**(17), 4777 (2008).

[17] Jin, X., Li, L., Chen, Z., Zhang, L., and Xing, Y., "Anisotropic total variation minimization method for limited-angle ct reconstruction," in [*SPIE Optical Engineering+ Applications*], 85061C–85061C, International Society for Optics and Photonics (2012).

[18] Gao, H., Yu, H., Osher, S., and Wang, G., "Multi-energy ct based on a prior rank, intensity and sparsity model (prism)," *Inverse problems* **27**(11), 115012 (2011).

[19] Chen, G.-H., Tang, J., and Leng, S., "Prior image constrained compressed sensing (piccs): a method to accurately reconstruct dynamic ct images from highly undersampled projection data sets," *Medical physics* **35**(2), 660–663 (2008).

[20] Szczykutowicz, T. P. and Chen, G.-H., "Dual energy ct using slow kvp switching acquisition and prior image constrained compressed sensing," *Physics in Medicine and Biology* **55**(21), 6411 (2010).

[21] Kim, K. S., Ye, J. C., Worstell, W., Ouyang, J., Rakvongthai, Y., Fakhri, G. E., and Li, Q., "Sparse-view spectral CT reconstruction using spectral patch-based low-rank penalty," *IEEE Trans. Med. Imaging* **34**(3), 748–760 (2015).

[22] Duda, R. O., Hart, P. E., and Stork, D. G., [*Pattern classification*], John Wiley & Sons (2012).

[23] Rumelhart, D. E., Hinton, G. E., and Williams, R. J., "Learning representations by back-propagating errors," *Cognitive modeling* **5** (1988).

[24] Wang, G. and Jiang, M., "Ordered-subset simultaneous algebraic reconstruction techniques (os-sart)," *Journal of X-ray Science and Technology* **12**(3), 169–177 (2004).